CLIMATE PATTERNS OF HABITABLE EXOPLANETS IN ECCENTRIC ORBITS AROUND M DWARFS

Yuwei Wang[1], Feng Tian[2], and Yongyun Hu[1]
[1] Laboratory for Climate and Ocean-Atmosphere Sciences, Department of Atmospheric and Oceanic Sciences,
School of Physics, Peking University, Beijing 100871 China; yyhu@pku.edu.cn
[2] Ministry of Education Key Laboratory for Earth System Modeling, Center for Earth System Science, Tsinghua University, Beijing 100084, China

ABSTRACT

Previous studies show that synchronous rotating habitable exoplanets around M dwarfs should have an "eyeball" climate pattern—a limited region of open water on the day side and ice on the rest of the planet. However, exoplanets with nonzero eccentricities could have spin–orbit resonance states different from the synchronous rotation state. Here, we show that a striped-ball climate pattern, with a global belt of open water at low and middle latitudes and ice over both polar regions, should be common on habitable exoplanets in eccentric orbits around M dwarfs. We further show that these different climate patterns can be observed by future exoplanet detection missions.

Key words: astrobiology – planetary systems – stars: individual (GJ 667C)

Online-only material: color figures

1. INTRODUCTION

Recent works suggest that habitable planets should be common around M dwarfs (Dressing & Charbonneau 2013; Gaidos 2013; Kopparapu 2013; Tuomi et al. 2014). The liquid water habitable zone of M dwarfs is typically at ∼0.1 AU (Kasting et al. 1993; Kopparapu et al. 2013). At this short distance, exoplanets are locked in spin–orbit resonance states by strong tidal forces. For planets with low-eccentricity orbits, the 1:1 resonance state (synchronous rotation) is the most likely configuration in which an exoplanet's rotation period is equal to its orbital period. In this case, one side of the planet faces its parent star permanently. Atmospheric general circulation models suggest an "eyeball" climate pattern (Pierrehumbert 2011; Edson et al. 2011, 2012; Heng & Vogt 2011; Wordsworth et al. 2011; Yang et al. 2013; Hu & Yang 2014), with a limited area of open ocean centered at the substellar point and complete ice coverage on the night side, and that the eyeball pattern remains even with a strong greenhouse effect and stellar radiation (Pierrehumbert 2011; Hu & Yang 2014).

However, an increasing number of observations indicate that many exoplanets have large eccentricities (Wright et al. 2011; Kane et al. 2012). Up to 2014 January, more than 40% of observed exoplanets had $e > 0.1$, and about 25% of observed super-Earths had $e > 0.1$ (Exoplanet Orbit Database), for example, $e \sim 0.97$ for HD 20782b (O'Toole et al. 2009) and $e \sim 0.4$ for super-Earth HD 181433b (Bouchy et al. 2009).

Eccentricity has important effects on exoplanets' climates (Dressing et al. 2010; Linsenmeier et al. 2014). For exoplanets around M dwarfs, one effect is the large contrast of stellar fluxes between the apoastron and periastron, and another is the spin–orbit resonance states caused by the strong tidal force. Williams & Pollard (2002) found that the Earth would remain habitable if its eccentricity was 0.4. Kataria et al. (2013) considered the effects of large variations in stellar flux and resonance states for hot Jupiters and found that climate patterns of hot Jupiters in eccentric orbits are qualitatively similar to those in circular orbits. Previous climate simulations of habitable exoplanets of M dwarfs (Wordsworth et al. 2011; Yang et al. 2013) studied non-synchronous rotating exoplanets in circular orbits, which is not self-consistent because such exoplanets

must be captured into synchronous rotation, according to orbit dynamics.

In this Letter, we consider the effects of both large variations of stellar fluxes and different spin–orbit resonance states on climate patterns, and we argue that both the eyeball and a striped-ball climate pattern are possible for habitable exoplanets on eccentric orbits around M dwarfs. We also show that these climate patterns will be detectable by future observations of exoplanets. The next section discusses theoretical predictions of spin–orbit resonance states based on orbit dynamics. Section 3 describes the numerical model, and Section 4 presents simulation results. Section 5 is the conclusion.

2. SPIN–ORBIT RESONANCE STATES

Define the spin–orbit resonance number $p = (\omega/n)$, where ω and n are the spin and orbital mean angular velocities, respectively. A solid exoplanet can be locked into any spin–orbit resonance state, with p being equal to an integer or a half integer (Murray & Dermott 1999; Dobrovolskis 2007). For example, the Moon has $e = 0.05$ and $p = 1$, and Mercury has $e = 0.2$ and $p = 1.5$. For potentially habitable planets Gl 581d and GJ 667Cc, it was estimated that the most likely resonance states are $p = 2$ (Makarov et al. 2012) and $p = 1.5$ (Makarov & Berghea 2014), respectively.

The probabilities of resonance states under different eccentricities, calculated following the methods in Dobrovolskis (2007), are shown in Table 1, and indicate that the most likely spin–orbit resonance states are determined by the planet's initial spin states. Although the most likely resonance state for a planet with low eccentricity is $p = 1$, for rapidly spinning planets with $0.15 < e < 0.3$ and $0.3 < e < 0.4$, the most likely resonance states are $p = 1.5$ and $p = 2$, respectively. For slowly spinning planets with $0.33 < e < 0.44$, the most likely resonance state is $p = 1.5$.

The decaying eccentricity timescale for an Earth-mass and Earth-size planet at 0.1 AU around a 0.3 solar mass star is about 3.6 Gyr, assuming a tidal dissipation Q factor of 10, similar to that of the Earth (Goldreich & Peale 1966; Rasio et al. 1996). In comparison, the timescale for an exoplanet to be captured into spin–orbit resonance states, including the synchronous rotation,

Table 1
Most Likely Climate Patterns for Different Eccentricity Ranges and Resonance States

Fast Spin Initial State			Slow Spin Initial State		
Eccentricity Range	Most Likely p Value	Most Likely Climate Pattern	Eccentricity Range	Most Likely p Value	Most Likely Climate Pattern
$0 \leqslant e \leqslant 0.15$	1.0	Eyeball	$0 \leqslant e \leqslant 0.33$	1.0	Eyeball
$0.15 \leqslant e \leqslant 0.3$	1.5	Striped-ball	$0.33 \leqslant e \leqslant 0.44$	1.5	Striped-ball
$0.3 \leqslant e \leqslant 0.4$	2.0	Eyeball			
$0.4 \leqslant e \leqslant 0.47$	2.5	Striped-ball			

is 7000 yr (Guillot et al. 1996; Rasio et al. 1996). Thus, habitable exoplanets in eccentric orbits with various spin–orbit resonance states should be common. Although previous theoretical works on orbit dynamics have established the connection between eccentricities and likely spin–orbit resonance states for close-in exoplanets, the climate patterns of such exoplanets have not been studied. The major purpose of this Letter is to study climate patterns with different resonance states for exoplanets with eccentric orbits based on theoretical predictions of orbit dynamics.

3. MODEL DESCRIPTIONS

In previous works (Yang et al. 2013; Hu & Yang 2014), the Community Atmosphere Model version 3, originally developed for Earth climate simulations at the National Center for Atmospheric Research (Collins et al. 2004), was used to simulate climates of habitable exoplanets around M dwarfs. In this work, we further modified the model by considering the variations of stellar insolation in an eccentric orbit.

Similar to previous works, an aqua exoplanet with a slab ocean and thermodynamic sea ice are considered in the model—ice formation and melting are solely determined by ocean surface temperatures with a default freezing/melting temperature of $-1.8°$. Planetary parameters (4.3 Earth masses, a 0.12 AU semi-axis, and a 28 day orbit period) identical to those of GJ 667Cc (Delfosse et al. 2012; Anglada-Escudé et al. 2013) are used in this work. For stellar radiation, we assume a blackbody spectrum with an effective temperature of 3700 K. The planetary atmosphere contains 1 bar of background gas (e.g., N_2) and 355 ppmv of CO_2. The control simulations have $e = 0.4$ and 90.5% of the solar constant (1367 W m^{-2}) when the planet is at 0.12 AU; thus, the orbital-averaged insolation at the substellar point is 1350 W m^{-2}. Zero obliquity is assumed. Sensitivity tests with different eccentricities and stellar radiation are discussed in Section 4. The model reaches equilibrium after 10 Earth years. Simulations typically run for 40 Earth years. The results shown here are based on averages over the last 10 yr of simulations. The initial location of the exoplanet is at the periastron and the initial longitude of the substellar point is 180°.

4. RESULTS

4.1. Climate Patterns

The left panels of Figure 1 show migrations of the substellar point with time, and the right panels show global maps of annual mean (averaged over one orbital period) stellar fluxes. The position of the substellar point depends on the spin angular velocity ω and the orbital angular velocity n. When $\omega > n$, the substellar point moves westward; when $\omega < n$, the substellar point moves eastward. ω is normally a constant, but n is greater near the periastron and smaller near the apoastron. For $p = 1$,

the substellar point moves back and forth near 180° longitude (Figure 1(a)), and the maximum of the annual mean stellar fluxes is located at 180° (Figure 1(b)). Note that although the spatial distribution of annual mean stellar fluxes in this case ($e = 0.4$) looks similar to that of the synchronous rotating exoplanets in circular orbits, it is different from the latter because the location of the substellar point is not fixed. For $p = 2$, although the substellar point moves over all longitudes during one orbit, there is a fixed relationship between the substellar point location and the orbital distance of the exoplanet—the exoplanet is always at the apoastron when the substellar point is at 0° longitude, and is always at the periastron when the substellar point is at 180° (Figure 1(e)). In addition, the substellar point in the $p = 2$ case also stays around 180° longitude much longer than near any other longitudes (Figure 1(e)). As the exoplanet approaches the periastron, n increases gradually and eventually exceeds ω, leading to an eastward movement of the substellar point for about five days, in contrast with the usually westward movement. When the exoplanet leaves the periastron, n decreases gradually and the eastward movement of the substellar point eventually returns to the normal westward movement. As a result, the orbit-averaged stellar radiation is much greater at 180° than at other longitudes (Figure 1(f)). For $p \geqslant 2.5$, the spin angular velocity is larger than the orbital angular velocity, even at the periastron. Thus, the substellar point always moves westward (Figure 1(g)). The Earth is a good example of this case. By contrast, for $p = 1, 1.5,$ and 2, the substellar point sometimes moves westward and sometimes eastward (Figures 1(a), (c), and (e)).

Two distinctively different climate patterns can be observed in the simulated annual mean surface temperature contours (Figure 2): an eyeball ($p = 1$ and 2) and a striped ball ($p = 1.5, p = 2.5,$ and all other values). For $p = 1$ (Figure 2(a)), the temperature contours are nearly concentric circles around 180° longitude. The highest temperature is above 300 K, while the lowest temperature (>200 K) is located in both polar regions. For $p = 2$ (Figure 2(c)), temperature contours above 280 K are close to concentric circles, whereas contours with lower temperatures extend eastward because of eastward heat transport by the westerly equatorial jet stream.

For $p = 1.5$ and 2.5 (Figures 2(b) and (d)), temperature contours become straight lines, consistent with the spatial distribution of stellar fluxes shown in Figures 1(d) and (h). The zonally non-uniform behavior in the highest temperatures in Figure 2(d) is due to non-uniform cloud distributions. Ice coverage and open-ocean distributions (not shown) are consistent with the surface temperature distributions in Figure 2. The relationship between a habitable exoplanet's climate pattern and its spin–orbit resonance state and eccentricity is summarized in Table 1.

Our simulations also show that the global mean surface air temperature of an eyeball planet can be 36 K lower than that
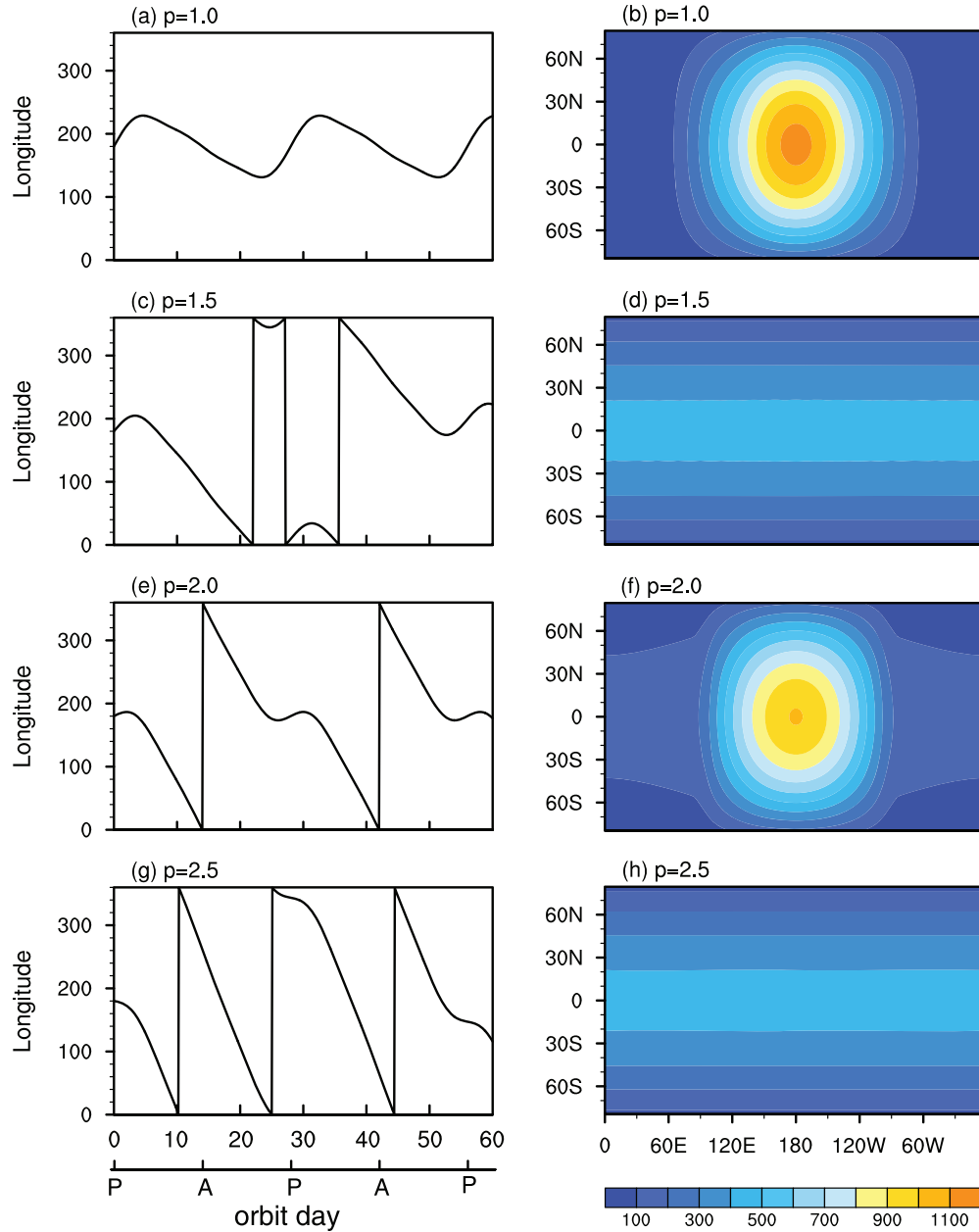
Figure 1. Left panels: migration of the substellar point for $e = 0.4$. Day 0 corresponds to the periastron, and the initial substellar point is at $180°$ longitude. The horizontal line at the bottom of the left panels shows the locations of the periastron (denoted by P) and apoastron (denoted by A). Right panels: stellar fluxes at the top of the atmosphere averaged over one orbital period for various p values. Units are W m^{-2}. The color interval is 100 W m^{-2}. Descriptions of this figure are in the main text.

(A color version of this figure is available in the online journal.)

of a striped-ball exoplanet if they receive identical annual mean stellar insolation because of planetary albedo effects. First, the sea-ice coverage of an eyeball planet can be up to 55%, in comparison with the $<18\%$ sea-ice coverage of a striped-ball planet. Therefore, a striped-ball planet has much lower surface albedo and thus absorbs more stellar radiation. Second, the cloud albedo on the day side of an eyeball planet is higher than that of a striped-ball planet because of a stronger day–night temperature contrast (Yang et al. 2013; Hu & Yang 2014), which causes strong convections and thus deep clouds on the day side.

Spatial patterns of the hydrological cycles are shown in Figure 3. For an eyeball exoplanet, the strongest precipitation, 430 mm per orbital year (5600 mm per Earth year), occurs in the warmest region. In contrast, the precipitation is <10 mm per

orbital year (130 mm per Earth year) on the night side. Spatial patterns of evaporation do not match those of precipitation. The location of the largest evaporation shifts slightly westward as a result of the substellar point movement (Figure 1(e)), which makes the east side produce denser clouds before the planet reaches periastron, where the evaporation is strongest, consistent with the results in Hu & Ding (2013). A wet area with precipitation exceeding evaporation is around $180°$ longitude, and a dry zone (evaporation exceeding precipitation) is in the surrounding region.

For a striped-ball exoplanet, precipitation is nearly zonally uniform and decreases with latitude. A zonal belt with a precipitation rate >120 mm per orbital year (1600 mm per Earth year) is between $30°$S and $30°$N, much broader than the
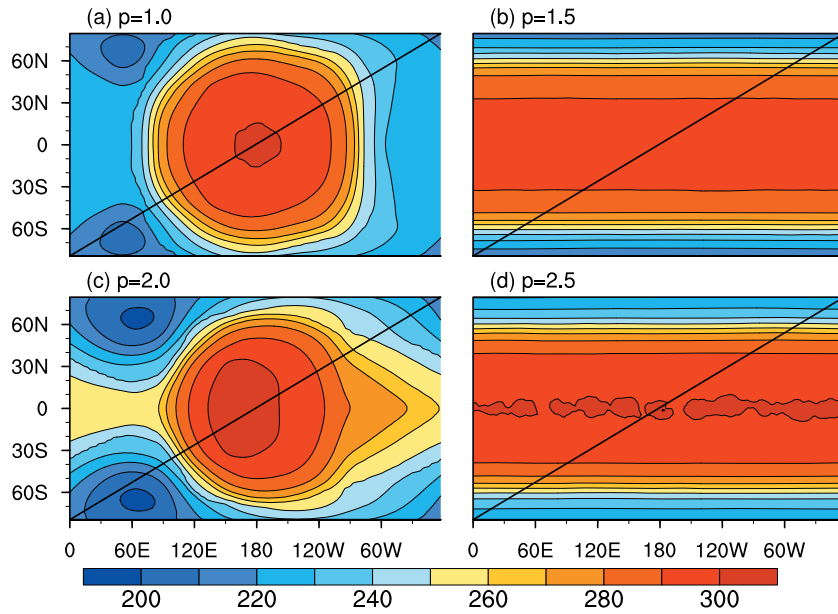
Figure 2. Surface air temperatures averaged over one orbital period for $e = 0.4$ and different spin–orbit resonance states. Units are K. The color interval is 10 K. Descriptions of this figure are in the main text.

(A color version of this figure is available in the online journal.)
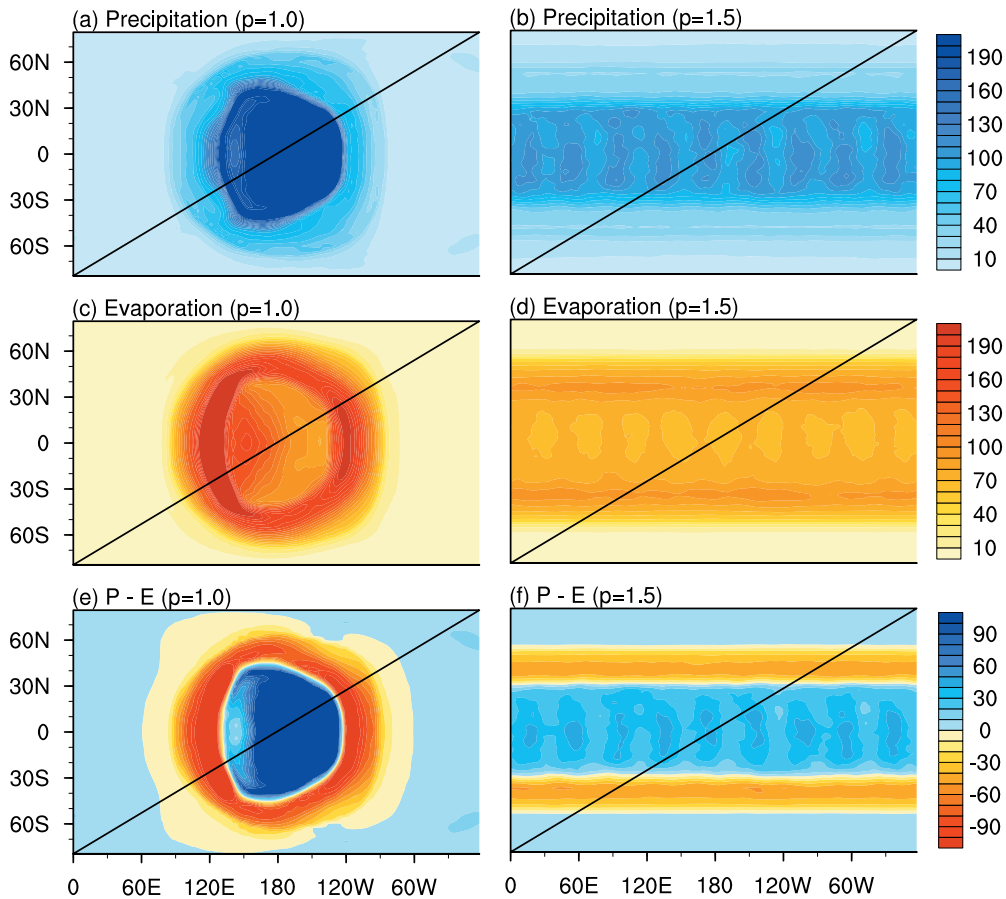

Figure 3. Patterns of precipitation and evaporation averaged over one orbital period for $e = 0.4$. Top panels: precipitation, middle panels: evaporation, and bottom panels: precipitation minus evaporation. Units are mm per orbital year. The color interval is 10 mm per orbital year.

(A color version of this figure is available in the online journal.)

inter-tropical convergence zone of Earth. The spatial pattern of evaporation is similar to the pattern of surface temperature. As a result, there is a wet zone between 30°S and 30°N and two dry zones between 30°N and 40°N in both hemispheres. The

dry zones here resemble Earth's subtropical dry zones, where continents are mostly deserts.

Simulations show that if the stellar radiation is increased from 0.9 to 1.1 times the solar constant, the climate pattern of
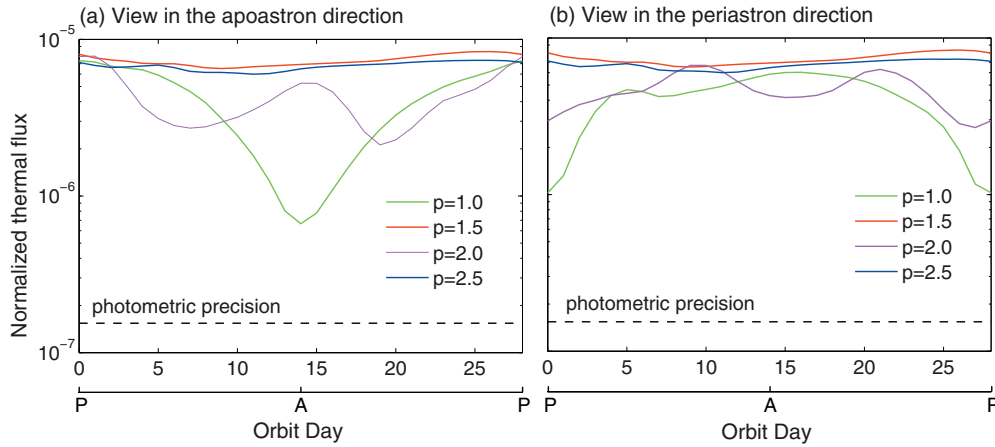
Figure 4. Thermal phase curves of habitable exoplanets around M dwarfs for different p values. Planetary thermal fluxes are normalized by stellar fluxes that are also integrated from 8 to 28 μm. The horizontal lines at the bottom show locations of the periastron and apoastron. Descriptions of this figure are in the main text.
(A color version of this figure is available in the online journal.)

a $p = 2$ planet changes from an eyeball to a striped ball. In comparison, the eyeball pattern remains for a $p = 1$ planet, even under strong stellar radiation (Hu & Yang 2014). In simulations with $e = 0.2$, the climate pattern for $p = 2$ is also a striped ball. Although zonal ocean heat transport could modify an eyeball climate pattern into a "lobster" pattern (Hu & Yang 2014), this effect would not change the striped-ball climate pattern.

4.2. Observations of Climate Patterns

The two climate patterns can be distinguished by observing thermal phase curves. Following Cowan et al. (2012) and Yang et al. (2013), the disk-integrated broadband thermal phase curves (integrated from 8 to 28 μm, which is within the range of the Mid-Infrared Instrument of the *James Webb Space Telescope*, *JWST*) are calculated assuming an edge-on orbit with zero obliquity. Figure 4 shows the normalized planetary thermal fluxes from an exoplanet at 6.8 pc (the distance of GJ 667Cc from Earth) with a 1 day *JWST* observation time. The normalized thermal phase curves from a striped-ball planet are on the order of 10^{-5} and have very weak variations ($<2 \times 10^{-6}$). In comparison, phase curves from an eyeball planet have much greater variations ($6 \sim 7 \times 10^{-6}$ for $p = 1$ and $4 \sim 5 \times 10^{-6}$ for $p = 2$). These are well above the photometric precision of *JWST* (1.5×10^{-7}) and thus are observable and identified by *JWST*. At the distance of Kepler 186f (151 pc), the photometric precision of *JWST* is 3.3×10^{-6}. Provided that the electric noise and stellar noise can be ignored, it would still be possible to recognize an eyeball planet.

Phase curves are different for different viewing angles. If one observes in the apoastron direction, an eyeball exoplanet with $p = 1$ looks brightest at the periastron when its day side is facing the observer, and looks dimmest at the apoastron when its night side is facing the observer (Figure 4(a)). For $p = 2$, the phase curve has two peaks, and the exoplanet looks bright at both the apoastron and periastron when its ocean side faces the observer.

If one observes in the periastron direction (Figure 4(b)), the phase curves for eyeball exoplanets are nearly reversed, except that phase-curve variations have weaker amplitudes. In addition, there is a weak minimum at day 6 for $p = 1$. This is because, although a broader open-ocean area can be observed at day 6 than at day 5, stellar insolation becomes weaker, which leads to lower thermal radiation.

5. CONCLUSIONS

Previous works have suggested that habitable exoplanets around M dwarfs have an eyeball climate pattern. Dynamic theory predicts that habitable planets on eccentric orbits around M dwarfs with non-synchronous rotation states are common. In this Letter, we show that a striped-ball climate pattern should be common for such planets. We also show that the two climate patterns can be distinguished by future *JWST* observations. Validations of the predicted relationship between climate patterns and spin–orbit resonance states of habitable exoplanets around M dwarfs should be a priority for future exoplanet observations.

REFERENCES

Anglada-Escudé, G., Tuomi, M., Gerlach, E., & Barnes, R. 2013, A&A, 556, A126
Bouchy, F., Mayor, M., Lovis, C., et al. 2009, A&A, 496, 527
Collins, W. D., Rasch, P. J., Boville, B. A., et al. 2004, NCAR Tech Note NCAR/TN-464 + STR (Boulder, CO: National Center For Atmospheric Research), 226
Cowan, N. B., Voigt, A., & Abbot, D. S. 2012, ApJ, 757, 80
Delfosse, X., Bonfils, X., Forveille, T., et al. 2012, A&A, 553, A8
Dobrovolskis, A. R. 2007, Icar, 192, 1
Dressing, C. D., & Charbonneau, D. 2013, ApJ, 767, 95
Dressing, C. D., Spiegel, D. S., Scharf, C. A., Menou, K., & Raymond, S. N. 2010, ApJ, 721, 1295
Edson, A., Lee, S., Bannon, P., Kasting, J. F., & Pollard, D. 2011, Icar, 212, 1
Edson, A. R., Kasting, J. F., Pollard, D., Lee, S., & Bannon, P. R. 2012, AsBio, 12, 562
Gaidos, E. 2013, ApJ, 770, 90
Goldreich, P., & Peale, S. 1966, AJ, 71, 425
Guillot, T., Burrows, A., Hubbard, W., Lunine, J., & Saumon, D. 1996, ApJL, 459, L35
Heng, K., & Vogt, S. S. 2011, MNRAS, 415, 2145
Hu, Y., & Ding, F. 2013, Sci. Sin-Phys Mech. Astron., 43, 1356
Hu, Y., & Yang, J. 2014, PNAS, 111, 629

Kane, S. R., Ciardi, D. R., Gelino, D. M., & von Braun, K. 2012, MNRAS, 425, 757
Kasting, J. F., Whitmire, D. P., & Reynolds, R. T. 1993, Icar, 101, 108
Kataria, T., Showman, A. P., Lewis, N. K., et al. 2013, ApJ, 767, 76
Kopparapu, R. K. 2013, ApJL, 767, L8
Kopparapu, R. K., Ramirez, R., Kasting, J. F., et al. 2013, ApJ, 765, 131
Linsenmeier, M., Pascale, S., & Lucarini, V. 2014, in EGU General Assembly 2014, Habitability of Earth-like planets with high obliquity and eccentric orbits: results from a general circulation model
Makarov, V. V., & Berghea, C. 2014, ApJ, 780, 124
Makarov, V. V., Berghea, C., & Efroimsky, M. 2012, ApJ, 761, 83
Murray, C. D., & Dermott, S. F. 1999, Solar System Dynamics (Cambridge: Cambridge university press)
O'Toole, S., Tinney, C., Jones, H., et al. 2009, MNRAS, 392, 641
Pierrehumbert, R. T. 2011, ApJL, 726, L8
Rasio, F., Tout, C., Lubow, S., & Livio, M. 1996, ApJ, 470, 1187
Tuomi, M., Jones, H. R. A., Barnes, J. R., & Anglada-Escude, G. 2014, MNRAS, 441, 1545
Williams, D. M., & Pollard, D. 2002, IJAsB, 1, 61
Wordsworth, R. D., Forget, F., Selsis, F., et al. 2011, ApJL, 733, L48
Wright, J. T., Fakhouri, O., Marcy, G. W., et al. 2011, PASP, 123, 412
Yang, J., Cowan, N. B., & Abbot, D. S. 2013, ApJL, 771, L45